2020

Characterization of a Novel Terahertz Chemical Sensor

Daniel J. Tyree
Wright State University

CHARACTARIZATION OF A NOVEL TERAHERTZ CHEMICAL SENSOR

A Thesis submitted in partial fulfillment of the
requirements for the degree of
Master of Science

by

DANIEL J TYREE

B.S. Wright State University, 2017

2020

Wright State University

WRIGHT STATE UNIVERSITY

GRADUATE SCHOOL

12/10/2020

I HEREBY RECOMMEND THAT THE THESIS PREPARED UNDER MY SUPERVISION BY DANIEL J TYREE ENTITLED CHARACTARIZATION OF A NOVEL TERAHERTZ CHEMICAL SENSOR BE ACCEPTED IN PARTIAL FULFILLMENT OF THE REQUIREMENTS FOR THE DEGREE OF MASTER OF SCIENCE.

_____

Ivan Medvedev, Ph.D.
Thesis Director

_____

Jason Deibel, Ph.D.
Chair, Physics

Committee on Final Examination:

_____
Ivan Medvedev, Ph.D.

_____
Brent Foy, Ph.D.

_____
Jason Deibel, Ph.D.

_____
Barry Milligan, Ph.D.
Interim Dean of the Graduate School

ABSTRACT

Tyree, Daniel J. M.S. Department of Physics, Wright State University, 2020.
Characterization of a Novel Terahertz Chemical Sensor

A recently constructed novel analytical tabletop terahertz (THz) chemical sensor capable of detecting a wide range of gases with high sensitivity and specificity was characterized to assess its performance over a range of operational parameters. The sensor was designed with an objective of quantifying composition of exhaled human breath, where target concentrations span part per trillion (ppt) to part per billion (ppb) level of dilutions. The sensor utilizes terahertz rotational spectroscopy of sampled gases for quantification of dilutions. The sensor occupies a volume of ~ 2 ft^3 and incorporates a coiled absorption cell, thermal desorption tubes, and all necessary electronic components necessary for autonomous operation. Coiled absorption cell minimizes the sensor footprint while maintaining a large path length for sensitive spectral measurements. Preconcentration aides the detection of compounds by removing the background gases which would negatively affect the absorption signal if present during spectral analysis. Spectral parameters of the sensor were studied to optimize its sensitivity. Efficiencies of preconcentration over a range of gas sampling parameters were determined by comparing concentrations measured by the sensor to concentrations of a reference gas mixture. The sensor was characterized in its ability to detect acetaldehyde, acetone, ethanol, isoprene, and methanol – all known breath analytes. These gases were chosen for their range of

volatility and absorption strength. Minimum detectable sample concentrations are well suited for breath sampling making this sensor a valuable new tool for environmental sensing and biosensing.

TABLE OF CONTENTS

TABLE OF CONTENTS (Continued)

LIST OF FIGURES

Page

LIST OF TABLES

Page

1. Introduction

Gas sensing, in both qualitative and quantitative operation, has a wide range of applications from industrial process monitoring [1]–[5] to personal medical diagnostics [6]–[11]and the demand for accurate and selective sensing is growing [5], [12], [13]. Specifically, medical diagnostic techniques from analysis of human breath show great potential for non-invasive measurements [8], [10], [14]–[17]. Exhaled human breath is rich in volatile organic compounds (VOCs) generated by metabolic processes in the body. By identifying and quantifying these metabolic products, a sense of a patient's health may be determined. However, many of these products are expressed at low concentrations presenting a challenge to reliable analysis.

In practice, there exist a variety of methods to analyze gas mixture constituents. Several popular methods are electrochemical sensors [7], [11], gas chromatography coupled to mass spectrometry (GC-MS) [18], [19], and optical spectroscopy [20], [21] means of detection. Each approach possesses advantages and weaknesses in terms of the diversity of compounds identified, the confidence in the detection or quantification of the gas, form factor, and duty cycle. One such method with considerable promise for breath analysis is a spectroscopic technique that probes the rotational motion of molecules in a gas [21]–[23]. Rotational spectroscopy studies a gas's response to a radiation source as the gas absorbs an incident photon to increase its rotational energy or emits a photon as the molecule relaxes from an elevated energy. Spectral features produced by this change

in energy are generally narrow, a few MHz, in relation to the bandwidth of a typical spectrometer, around 100 GHz, providing many resolution elements for selective sensing [24]–[26] . Additionally, these features are often numerous, providing many opportunities for detection. The abundance of resolvable features ensures significant redundancy for accurate detection, minimizing the likelihood of a false positive detection. From these spectral features, the quantity of interacting molecules in a gas can be derived accurately. These traits make it an ideal technique for gaseous chemical sensing.

Recently, a novel terahertz rotational absorption, chemical sensor has been constructed to facilitate the identification and quantification of VOCs in breath. For accurate quantitative rotational spectroscopy measurements of these VOCs, a thorough understanding of both the spectroscopic processes used to quantify the gas and the treatment of a gaseous sample prior to analysis is required. Targeted towards detection of trace gases in breath samples, additional steps are required to ensure the sample delivered for analysis is under ideal conditions. As breath includes relatively large amounts of nitrogen, oxygen, and water vapor. Separation of the compounds of interest from these three species greatly improves the sensitivity of the sensor [21]. One such method of separation is borrowed from thermal desorption GC-MS sensors which utilize a sorbent material to trap target gases while rejecting others [18]. Preconcentration in this manner varies significantly depending on the parameters of the adsorption process, such as the sorbent temperature when trapping or releasing a sample.

The sensor described here incorporated a 7.8 m long absorption cell for sensitive spectral measurements. To minimize the footprint of the sensor, this long cell was coiled into a solenoid. Characterization of the spectroscopic performance and preconcentration process

was performed in order to determine the relationship between a spectroscopically measured, preconcentrated sample to the source gas.

2. Background

2.1 Rotational Absorption Spectroscopy

For measurements of gas samples near room temperature, the rate of spontaneous emission is very low in the terahertz (THz) range which makes emission spectroscopy unviable [24]–[26]. Instead, the neutral gas is probed by studying its interaction with generated photons. A gas interacts with the incoming radiation by electromagnetic forces between the molecule and the fields of the photon. The most likely, and strongest interactions occur when a molecule has a permanent electric or magnetic dipole moment. The field of the photon applies a torque to the dipole causing a change in the molecule's rotational energy. In practice, this is done by sending a monochromatic beam of radiation through the gas and measuring the response by collecting the outgoing radiation along the path of the beam. In the presence of an interacting gas molecule, the incident photons are absorbed by the gas causing a reduced signal at the receiver. This produces a drop in radiation power for specific frequencies corresponding to the gas. Generally, for rotational spectroscopy, these frequencies are in the THz, range situated between the microwave and infrared regions in the electromagnetic spectrum.

2.2 Rotational Energy Levels

Calculation of specific absorption frequencies requires an understanding of the quantized energy structure of the molecule. Rotational energies are described by three molecule specific constants, A, B, and C, which are commonly given in units of GHz. They are

determined from the principal moments of inertia for the molecule, I_a, I_b, and I_c [24]–[26]. The A constant is given as: $A = \frac{h}{8\pi^2 I_a}$ $(equ. 1)$ [25]

where A = the rotational constant associated with the principal moment of inertia, I_a

h = Planck's constant.

I_a = the principle moment of inertia

Constants B and C are calculated in the same manner by replacing the principal moment of inertia, I_a, with the corresponding principal moment. The calculation of energies from these constants depends on the structure of the molecule and the rigidity of its atomic bonds. For diatomic molecules or rigid linear molecules in their vibration ground state, symmetry about a single axis gives principle moments of inertia as $I_a = 0$ and $I_b = I_c$ [24]–[26]. The energies of the molecules are determined by the B constant and rotational quantum number, J, which denotes the rotational energy level. These rotational energies are given by: $E(J) = hBJ(J + 1)$ $(equ. 2)$ [25]

where $E(J)$ = the rotational energy of a molecule

B = the rotational constant if the principal moment of inertia, I_b

J = the rotational quanta number

Less rigid molecules have their shape distorted at higher rotational energies resulting in changes in the principal moments of inertia. The energies for these molecules are determined by a similar equation including higher order terms with respect to rotational quantum number to correct for these distortions [24]–[26].

Photons, when absorbed by a molecule, cause the energy of the molecule to increase. As these energies are quantized, for absorption to occur, the energy of the photon must be precisely the difference in energy between the initial and final energy state of the molecule. For dipole interactions, not all changes in energy are allowable. Selection rules for dipole allowed rotational transitions of a diatomic molecule hold that the change in energy can only be between adjacent states, $\Delta J = \pm 1$ [24]–[26]. This means the frequencies of photons capable of being absorbed by a gas must correspond to the energy difference between two adjacent rotational energy levels. Photon frequency is given as:

$$f = \frac{E(J+1)-E(J)}{h} = 2B(J+1)\ (equ.3)$$ [25]

where f = the photon frequency of a rotational transition

J = the rotational quantum number of the lower rotational state

This relationship shows that the expected frequencies for rotational energy transitions will occur at evenly spaced frequencies separated by $2B$. For less rigid species, the transition spacing is still largely $2B$ with deviations caused by the higher order distortion terms [24]–[26].

For other non-linear molecules, the principal moments of inertia vary more from one another which complicate the expression for energy [24]–[26]. Non-linear molecules are divided into three categories, spherical tops, asymmetric tops, and symmetric tops. Spherical tops have molecular structure such that the principal moments of inertia are all equal [24]–[26]. This structure also means that there is no permanent dipole moment for the photon to interact with. As such, the spherical top does not have electric dipole allowed rotational spectra [24]–[26]. Asymmetric tops have non-zero principal moments

of inertia none of which are equal to each other [24]–[26]. This complexity prevents an analytical form for the rotational energies to be determined for most J [24]–[26] and must be calculated on an individual basis. Symmetric tops fall into two categories; prolate, when $I_a < I_b = I_c$, and oblate, when $I_a = I_b < I_c$ [24]–[26]. The addition of a third non-zero, moment of inertia requires that the energy state be tracked with an additional quantum number. Quantum numbers J and K are used to represent the total angular momentum and its projection along the top axis, I_a for prolate tops and I_c for oblate tops, respectively [24]–[26]. The projection quantum number, K, is constrained such that it cannot be greater in magnitude than J [24]–[26]. Energies for a rigid prolate top are given by: $E(J,K) = h[BJ(J+1) + (A-B)K^2]$ $(equ. 4)$ [25]

where K = the quantum number corresponding to the projection of the total angular momentum.

The energies of the oblate top are also determined equation 4 by replacing the constant A with C [24]. Less rigid molecules have a similar higher order J term to account for distortion at higher rotational energies. They also possess similar selection rules to the diatomic molecules requiring that $\Delta J = \pm 1$. Additionally, the quantum number K is also constrained such that it does not change, $\Delta K = 0$ [24]–[26]. Since the K term must remain unchanged between the two rotational states, these rules generate rotational transition frequencies of the same form as equation 3 for the linear molecule.

2.3 Measurement of a Rotational Transition

As probe radiation is swept through an interacting gas, a fraction of photons with frequency near or equal to the rotational transitions determined by equation 3 are

absorbed. This absorption produces narrow lines of signal about the transition frequency, called absorption lines [24]–[26]. The fraction absorbed determines the change in radiation power transmitted through the gas. Change in power depends on several molecular specific factors as well as the number of molecules in the path of the radiation. Transmitted power through an absorbing gas is given by the Beer-Lambert Law of attenuation: $P(f) = P_0(f)e^{-\alpha(f)c_g L}$ $(equ. 5)$ [26]

where P = the power transmitted through the gas

P_0 = the baseline power

α = the absorption coefficient

c_g = the concentration of the absorbing gas

L = the path length of the radiation

f = the frequency of the probe radiation

The absorption coefficient, α, is frequency dependent and is determined by the difference in the number of molecules in the lower and upper energy state, the quantum mechanical probability of the transition, and gas temperature. Frequency dependence of α corresponds to a combination of Gaussian and Lorentzian distributions centered about the frequency of the transition given by equation 3. The combination of these distributions is known as a Voigt distribution which has a Gaussian core and Lorentzian wings [27]. Commonly the largest Gaussian contribution to this profile comes from Doppler broadening, the Doppler shift in the incident photon caused by thermal motion of the gas molecules [24]–[26]. This shift causes the frequency of the photon relative to the

molecule to appear to have slightly smaller or larger frequencies than the source which enables photons with frequencies near but not equal to the transition frequency to be absorbed [25]. As the Doppler shift is determined by the thermal velocities of the molecules in the sample, absorbed photons are distributed along a Gaussian distribution with a full width at half the maximum amplitude (FWHM) known as the Doppler width of the line. This width is given by $FWHM = f_0\sqrt{\frac{8k_bTln(2)}{mc^2}}(equ.6)$ [25]

where $FWHM$ = the full width at half maximum of the absorption line

f_0 = the central frequency of the transition line

k_b = the Boltzmann constant

T = the average gas temperature in Kelvin

m = the mass of the molecule

c = the speed of light in vacuum

If excessive power is applied to the sample, power saturation can be observed experimentally [24]–[26]. Power saturation distorts the population between the two energy levels such that the difference is not thermally determined. This also distorts the absorption coefficient and reduces the measured absorption [24]–[26]. If the gas is not saturated with radiation power, the Lorentzian contributions primarily come from two sources, one is natural broadening due to the uncertainty in the exact energy of either rotational level caused by the Heisenberg uncertainty principle, the other, pressure broadening, comes from collisions with other gas molecules perturbing the structure of the molecule and shifting the energy states [24]–[26]. Absorbed photons shifted by these

effects are distributed along separate Lorentzian distributions with each width specific to the transition or molecular collisional partners [25]. Generally, near room temperatures, the Doppler broadening contribution are much larger than the natural broadening. This leaves the overall frequency dependence of the absorption coefficient as a mixture of Doppler and pressure broadening.

In cases where the absorption is sufficiently small, the exponential in equation 5 can be approximated as a linear change in power with respect to the absorption coefficient and path length. In these cases, the attenuation of the gas from the Beer-Lambert law can be approximated as: $P(f) = P_0\big(1 - \alpha(f)c_g L\big)\ (equ. 7)$

This simplified relationship between absorption coefficient and the transmitted power enables a more direct assessment of the gas concentration. Using this relation, the fractional transmission is found by taking a ratio of the measured absorption power and the baseline power. Fractional transmission exposes the absorption coefficient as an inverted Voigt profile scaled by concentration and path length and vertically offset by from zero. With knowledge of the path length, the concentration can be determined from the area of the Voigt profile.

2.4 Frequency Modulation Spectroscopy

Often an experiment is designed such that the absorption is small enough, compared to the baseline, to employ equation 7 for simpler analysis. This is generally the case for sensing gas metabolites in human breath. However, when the absorption signal is very small, comparable to the noise of the photon detector, then the gaseous concentration is difficult to accurately reconstruct. Additionally, the baseline power of the source in the

region of a transition may have significant slope and curvature complicating the analysis of the weak absorption line. In these cases, an amplification technique is employed to selectively enhance the signal separately from the noise and reduce the impact of the baseline power via frequency modulation (FM) spectroscopy. This method rejects 1/f noise on the measured power and applies a derivative-like effect to remove lower order terms of the power baseline signal [28]–[31].

Frequency modulation spectroscopy employs an oscillating waveform for the probe radiation. The frequency of the monochromatic radiation is modulated about a central frequency at a fixed rate and amplitude. The time dependent frequency of the source is given by: $f_s(t) = f_0 + f_d sin(\omega_m t)$ $(equ. 8)$ [30]

where f_s = the frequency of the source radiation

f_0 = the central frequency of the modulation

f_d = the amplitude of the modulation

ω_m = the rate of modulation

t = the time after setting the central frequency

The central frequency of the radiation source is then slowly, compared to the modulation rate, swept through the frequencies of a rotational transition. Modulation of the source causes a time dependent attenuation of the power transmitted through the gas corresponding to the frequencies absorbed by the gas. This gives the power transmitted as the combination of equations 7 and 8. The time dependent transmitted power for a given central frequency is: $P(f_0, t) = P_0\big(1 - \alpha\big(f_0 + f_d sin(\omega_m t + \varphi)\big)L\big)$ $(equ. 9)$ [30]

When the absorption coefficient is zero, for frequencies far from a transition, the time dependence of the transmitted power is negated, and the transmitted power is near constant. In the presence of an absorbing transition, the oscillating frequency is transformed into oscillations of the transmitted power depending on the strength and width of the absorption coefficient. This signal can be broken into a sum of components of integer harmonics of ω_m [32]. When the signal is passed into a phase-lock-in amplifier, the reference frequency of the amplifier is matched to one of these harmonic frequencies. The lock-in amplifier then takes the oscillating signal and beats it with the reference frequency returning two beat frequencies, the sum of the source frequency and the reference and the difference [33]. By high-pass filtering, only the low frequency signal from the difference in the source and reference frequencies are preserved. With a very low cutoff frequency, the signal is passed only when the source frequency and reference are nearly the same. In this process, unwanted frequencies and noise from the transmitted signal are quenched while the desired frequency is amplified [33]. With low pass filtering, the steady state output from the amplifier is dependent on the central frequency of the source radiation, gas concentration, shape of the absorption coefficient, rate of modulation, the harmonic reference, and significantly dependent of the amplitude of modulation.

For the n^{th} harmonic as a reference, if the modulation amplitude is much smaller than the width of the absorption transition, the output signal is approximately the n^{th} derivative of the absorption coefficient [32]. Typically, small modulation amplitudes are not used as the signal recoverable for a given harmonic is greater at amplitudes comparable to the line width [30]. For large modulation amplitudes, as long as the amplitude is on the order

of the width of the transition, the shape still resembles the derivative, however there are significant deviations preventing a direct derivative approximation. The derivative-like nature of the n^{th} harmonic signal is advantageous for its suppression of the curvature of the baseline. For example, if the 2^{nd} harmonic is used as reference, the output baseline signal has the offset and linear terms approximately removed and the quadratic terms of the baseline are converted into an offset in the amplified signal. This suppression simplifies the assessment of a measured transition [27], [30]. Combined, the baseline suppression and noise rejection enable an assessment of a weak spectral line improving the sensitivity of detection.

3. Methods

3.1 Sensor Operation

The novel gas sensor characterized in this work was a near standalone device containing most necessary components onboard for processing and performing spectroscopic analysis of a gaseous sample. A tablet computer was used to issue commands and collect the measured spectral data for quantification of the gas. Quantification was done by linearly fitting a reference library spectrum to the measured data. The sample processing and analysis included a metered draw of the sample into the sensor, preconcentration of the gas sample to separate background atmospheric compounds from the remaining sample, gas routing to evacuate previous samples and deliver the current sample, and THz spectroscopic analysis of the delivered gas.

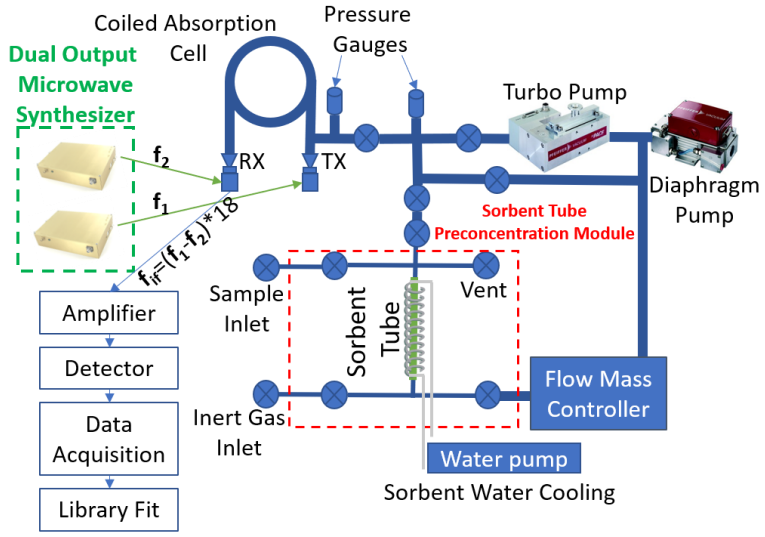

Fig. 1 A diagram of the gas sensor and detection routine. A flow mass controller sampled set volumes of gaseous sample for preparation in an onboard sorbent based preconcentration module. The preconcentrated sample was delivered to the absorption cell for analysis by a THz radiation source receiver pair. Output spectra were recorded by an external computer for quantification by a fit to prerecorded reference spectra.

A notable component of the sensor was the novel absorption cell. The absorption cell consisted of a 7.8 m length of stainless-steel tubing coiled into a solenoid. Coiling of the cell minimized the overall footprint of the sensor while maintaining a large path length. The longer path length increased the strength of the absorption signal as seen in equations 5 and 7 which increased the sensitivity of gas detection. A caveat to this cell shape came in the form of a significant frequency dependence on the transmitted power which caused some frequencies to transmit little to no power.

To optimize and define the performance of the sensor, an effort was undertaken to characterize the transmission of radiation through the cell and the performance of the preconcentration process. The results of this characterization were used to optimize sensor configuration for optimal performance. To understand the relevance of the optimized parameters, the operational routine of the sensor is explained in detail below.

1. Gas was sampled by an OMEGA FMA-6500 flow mass controller [34] backed by a Pfeiffer MVP 006 diaphragm pump [35] which drew a metered gas sample into the sensor. A flow mass controller allowed a configurable sample volume to be drawn in at atmospheric pressures at a controlled rate. Once drawn into the sensor, the meter drew the gas through the sorbent tube in the preconcentration unit.
2. Preconcentration of the gas sample was performed by drawing a sample through a custom thermal desorption (TD) tube consisting of a combination of Tenax GR and Carbograph 5TD. This sorbent material combination was selected for the hydrophobic nature of the sorbent materials and a wide range of sensitivity to volatile compounds [36]. The sorbent material selectively trapped gas molecules of interest while allowing background gases such as atmospheric oxygen or nitrogen pass

through. It was assumed that the adsorption of different gases in a sample were independent of one another so long as the concentration was low enough to not saturate the sorbent material. During this process, the tube was cooled by chilled water driven by a peristaltic pump from an external reservoir containing a mixture of ice and water. Cooling allowed the room temperature gas to be trapped more efficiently.

3. Once the gas sample had been loaded onto the sorbent tube, the headspace of the tube was evacuated to remove any remaining sample or background gases. This was done first by pumping on the backside of the sorbent tube with the diaphragm pump. One sided pumping with gas flow in the same direction as tube loading was expected to drive any remaining sample into the sorbent material and minimize potential stripping of the sample from the material by a large pressure swing when pulling a higher vacuum prior to sample delivery. After this initial pumping was completed, a Pfeiffer HiPace 10 [37] turbo-drag-pump was employed to pull a high vacuum on both sides of the sorbent tube.
4. Release of the trapped sample from the sorbent tube was performed in a manner differing from typical TD tube operation. In typical operation, the tubes are heated to a high temperature while a carrier inert gas (helium or nitrogen) flows through the tubes to carry the released gases to the quantitation system. This gas flow also helps to reduce decomposition of the sorbent material at the higher temperatures. Instead, the trapped gas was released directly into vacuum without a carrier gas. The evacuated sorbent tube was opened to the absorption cell, which had been previously evacuated by the turbo-drag-pump to a high vacuum. The tube was then heated to a

lower set temperature, commonly 140 C, to desorb the trapped gases into the cell with less risk of decomposing the sorbent material. As the gas was released from the sorbent tube, it filled the evacuated chamber. Once a set temperature was reached, the tubes were held at temperature for a length of time determined by the operator, often two to three minutes. After this time had elapsed the absorption cell was shut off from the sensor isolating the preconcentrated sample inside.

5. After delivery of the preconcentrated sample, the sorbent tube underwent a conditioning step to prepare for the next gas sample. This was done, similar to typical TD tube operation, by flowing an inert gas through the tube, in this work helium, while heating the tube to a high temperature, 220 C. The gas flow and high temperature promoted any remaining trapped gases back into the gas phase and flushed them out of the tube. The inert gas also protected the sorbent tube from thermal damage at the higher temperature. Conditioning temperature was maintained for an excessive amount of time to ensure the tubes had minimal sample carried over, typically 10 minutes. Inert gas flow was maintained throughout this process until the heating had stopped and the tubes had cooled sufficiently to prevent thermal damage.
6. Simultaneous to the conditioning step, the isolated gas in the absorption cell was probed by a THz radiation source. The source was a linearly polarized, solid-state, THz frequency emitter with range 0.220-0.330 THz driven by a microwave synthesizer both manufactured by Virginia Diodes Inc (VDI) [38]. The synthesizer generated frequencies from 7 to 12 GHz which were multiplied by a factor of 18 up to THz frequencies by solid state multipliers in the source. The emitted radiation was collected by a linearly polarized, solid-state heterodyne receiver also from VDI and

driven by another microwave synthesizer. Source radiation was collimated to probe a larger cross-section of the gas and the beam was refocused onto the receiver after traversing the cell. The two synthesizers were offset by 93 MHz and swept synchronously through selected frequencies. Input frequency to the receiver was multiplied by the same factor as the source and the frequency from the source was mixed in the heterodyne manner with this upconverted frequency. The result of mixing the offset signals was an output intermediate frequency equal to the offset of the synthesizers multiplied by 18, 1.674 GHz, which was amplified by a Mini Circuits ZX60-3011+ amplifier [39]. Frequency modulation described in section 2.4, was employed to recover weak spectral lines. The source frequency was modulated at 35kHz with a depth of 400 kHz. The FM signal was passed through the receiver and amplifier into an Anfatec lock-in amplifier which demodulated the 2^{nd} harmonic signal [40]. This demodulated signal was passed to a National Instruments Data Acquisition board which digitized the signal recorded by the controlling computer [41].

7. Demodulated spectra, recorded by the computer, were used to determine the concentration of each compound probed. This was done by a least squares regression to fit prerecorded library spectra to the experimental data, described in section 3.2. The results of this fit were used to determine the partial pressure of each compound in the sample. Partial pressures were used to determine the parts-per concentration (ppx) of compounds in the original sample.

3.2 Spectral Data Acquisition and Library Fitting

THz rotational lines were collected using the THz source, receiver, and microwave synthesizers described in part six of the sensor operational routine. The available spectral range of the source-receiver pair was 0.220 to 0.330 THz with typical spectral resolution of <50 kHz. This large range and fine resolution resulted in long sweep times, if the entire spectral range was collected for each sample. To accelerate data acquisition, a set of 5 MHz wide frequency snippets were probed in the vicinity of prominent spectral features in order to detect and quantify molecules in the gaseous sample. This also allowed regions of little to no absorption to be bypassed. Frequency snippets were chosen such that the center of each snippet matched that of a rotational transition of a chosen molecule. For each molecule selected, three snippets were chosen to be recorded. This enabled some redundancy in the case a rotational line belonging to a different molecule may have overlapped with one of the selected lines. The triplicate snippets also enabled reasonable redundancy in the case of an overlapping line from some other species.

Due to the 2^{nd} harmonic FM spectroscopy signal, direct assessment of the absorption line was challenging. This stems from the deviation from the 2^{nd} derivative line shape caused by a relatively large depth of modulation. To overcome this, 2^{nd} harmonic rotational spectra are analyzed by fitting to a prerecorded library for each compound under study.

Library fitting was suitable when the concentration of the gas was such that the gas remained optically thin and the pressure was low enough that collisional broadening was not significant. Under these conditions the rotational transition lines were considered to be Doppler limited and true absorption line shape was Gaussian with the width of the line depending only on the Doppler width of the gas shown in equation 6. Doppler limited

spectra for a given compound had fixed widths for a given gas temperature. This produced absorption lines whose widths were consistent, and, in the low absorption limit, whose amplitude varied linearly with concentration according to equation 7.

The linear relation between concentration and line amplitude enabled a simple scalar comparison between two lines of a compound at different concentrations to determine the relative concentration. This enabled the quantification of an experimental spectrum when the amplitude was compared to a spectrum of known concentration. As the volume of the gas in the absorption cell was fixed by the dimensions of the cell, the spatial concentration of a pure gas spectrum was proportional to the pressure of the pure gas in the cell. This pressure was easier to use as a reference for comparing to a partial pressure of a compound in a mixture held in the same volume. The concentration of an atmospheric sample was determined from the partial pressure derived from the fit. This pressure was used with experimentally measured parameters such as, gas temperature, sample volume, cell path length, and volume to determine the concentration in the sample. For a volume of gas sampled at room temperature in atmosphere, the concentration was derived from the ideal gas law by converting the measured pressure into the number of molecules in the sample. The ideal gas law was given as:

$PV = Nk_bT$ $(equ. 10)$ [42]

where P = the pressure of a gas in a volume

V = the volume of the gas

N = the number of molecules in the gas

k_b = the Boltzmann constant

T = the temperature of the gas

The number of molecules of a measured compound were divided by the total number of molecules in the sampled volume in atmosphere. From this ratio, the volumetric concentration of a gas at room temperature was as: $ppx = \frac{p_{mol}V_{cell}}{T_{mol}} \frac{T_{room}}{p_{atm}V_{sample}}$ $(equ. 11)$

where ppx = the volumetric concentration of the sample

p_{mol} = the pressure of the compound in the sample

V_{cell}= the volume of absorption cell

T_{mol} = the temperature of the gas sample in the absorption cell in Kelvin

T_{room} = the temperature of the atmospheric gas sample in Kelvin

p_{atm} = the atmospheric pressure

V_{sample} = the sampled volume of gas.

The fit for the sample pressure consisted of a least-squares regression to a combination of the prerecorded library spectra and a polynomial baseline. All frequency snippets for a given molecule were fitted simultaneously to a corresponding library, each with a separate baseline polynomial but all sharing the same amplitude to best match the library. The regression was performed by generating a design matrix of the reference library and frequencies of the measured snippets, where the number of columns, n, was equal to one plus the number of snippets to be fit multiplied by the baseline polynomial order plus one and the number of rows, m, was the total number of data points in all the snippets. The design matrix was then used to solve the system; $\hat{A}\vec{c} = \vec{b}$ $(equ. 12)$ [43]

where $\hat{A}$ = the m by n design matrix of frequencies and the library data

$\vec{c}$ = the fit coefficient vector

$\vec{b}$ = the experimental data vector

The design matrix, $\hat{A}$, was represented as a block matrix with blocks corresponding to each snippet along the diagonal and one column of library values for each snippet. The coefficient vector, $\vec{c}$, consisted of sub vectors with coefficients for the baseline terms for each snippet and a scalar applied to the reference library. In a similar form, the data vector, $\vec{b}$, consisted of sub vectors containing the spectral data of each snippet. Typically, there were three snippets of data, each with 102 data points, and a quadratic baseline was used, generating a 10 by 306 matrix. This matrix and these vectors are shown in block form as;

$$\hat{A} = \begin{bmatrix} \hat{S}_1 & 0 & 0 & \vec{L}_1 \\ 0 & \hat{S}_2 & 0 & \vec{L}_2 \\ 0 & 0 & \hat{S}_3 & \vec{L}_3 \end{bmatrix}_{m\times n}, \vec{c} = \begin{bmatrix} \vec{C}_1 \\ \vec{C}_2 \\ \vec{C}_3 \\ \alpha \end{bmatrix}_{n\times 1}, \vec{b} = \begin{bmatrix} \vec{D}_1 \\ \vec{D}_2 \\ \vec{D}_3 \end{bmatrix}_{m\times 1} \quad (equ. 13)$$

where $\hat{S}_1$ = a block matrix with rows equal to the number of data points in the first snippet and columns equal to the order of the baseline polynomial plus one

$\vec{L}_1$ = a vector of the library line for the first snippet with a number of rows to match the experimental snippet

$\vec{C}_1$ = a vector of baseline coefficients corresponding the fit baseline of the first snippet with rows equal to the baseline polynomial order plus one

α = the global scalar that is applied to the library to match the data

$\vec{D}_1$ = the experimental data in the first snippet.

m = the number of datapoints in all snippets

n = the number of all baseline coefficients plus one

The design matrix, $\hat{S}_i$, for each matrix held powers of the frequency values contained in each snippet. It and each of the other vectors were populated with library and data values according to:

$$\hat{S}_1 = \begin{bmatrix} 1 & x_0 & {x_0}^2 \\ \vdots & \vdots & \vdots \\ 1 & x_{101} & {x_{101}}^2 \end{bmatrix}, \vec{L}_1 = \begin{bmatrix} L(x_0) \\ \vdots \\ L(x_{101}) \end{bmatrix}, \vec{C}_1 = \begin{bmatrix} c_0 \\ c_1 \\ c_2 \end{bmatrix}, \vec{D}_1 = \begin{bmatrix} D(x_0) \\ \vdots \\ D(x_{101}) \end{bmatrix} (\ equ. 14) \text{ [43]}$$

where x_i = the frequency of each data point in a snippet

L = the library value of the corresponding frequency

c_0 = the offset term of the baseline polynomial

c_1 = the coefficient of the linear term of the baseline polynomial

c_2 = the coefficient of the quadratic term of the baseline polynomial

D = the data value of the corresponding frequency

The least squares solution to the overdetermined system of equations in equation 12 was found by solving the normal equations: $\vec{c} = \left(\hat{A}^T \hat{A}\right)^{-1} \hat{A}^T \vec{b}$ $(equ. 15)$ [43]

where $\hat{A}^T$ = the transpose of the matrix $\hat{A}$

The error in the resulting fit coefficients was determined from the covariance of the design matrix and the sum of the square of the residuals between the fit and the data. The error in a fit coefficient was found as: $\overrightarrow{\delta c_i} = \sqrt{\frac{\sum_{j=1}^{m}\left(\vec{b}_j - [\hat{A}\vec{c}]_j\right)^2}{m-n}\left[\left(\hat{A}^T\hat{A}\right)^{-1}\right]_{ii}}$ $(equ. 16)$ [44]

where $\overrightarrow{\delta c_i}$ = the error of the i[th] coefficient of $\vec{c}$

$\vec{b}_j$ = the j[th] value of the data vector

$\left[\hat{A}\vec{c}\right]_j$ = the j[th] value of the fit vector

$\left[\left(\hat{A}^T\hat{A}\right)^{-1}\right]_{ii}$ = the i[th] value along the diagonal of the square matrix $\left(\hat{A}^T\hat{A}\right)^{-1}$

Baseline polynomial terms ensured that the most robust match of the experimental line to the library was found in cases where FM spectroscopy failed to suppress all the baseline. From the global library scalar, the partial pressure of the experimental line was determined. Assuming the library pressure was low enough that equation 7 was applicable, had a zero-power baseline, and had been normalized to unit path length and gain, the product of the library pressure and the fit scalar term was proportional to the partial pressure of the corresponding compound. This proportionality depended on the experimental path length and any gains applied to the signal and had the form:

$\alpha p_{lib} = p_{mol} L g$ $(equ. 17)$

where α = the fit scalar

p_{lib} = the pressure of the library

p_{mol} = the partial pressure of the molecule being probed

L = the path length of the cell

g = the gain applied to the experimental signal

By rearranging equation 17 and inserting into 11, the concentration of the probed chemical was found by: $ppx = \frac{\alpha}{Lg}\frac{p_{lib}}{p_{atm}}\frac{T_{room}}{T_{cell}}\frac{V_{cell}}{V_{sample}}$ $(equ. 18)$

3.3 Library Development

To create reference libraries for fitting, selected gases were put into the absorption cell at a pressure sufficient for robust spectral signal, typically around 1 mTorr. Pressures were chosen such that the absorption was low enough for linear approximation of the absorption, equation 7, and there was no power saturation. The gas samples used for this purpose were prepared by placing a volume of spectroscopic grade liquid into a special vacuum flask. The flasks were submerged in liquid nitrogen until all the liquid has frozen. The headspace of each flask was evacuated using a high vacuum pump to remove any atmospheric gas from the flask. Once a good vacuum was achieved, the sample volume was sealed to maintain the vacuum in the flask. The flask was then removed from the liquid nitrogen so the liquid, left to warm to room temperature, evaporated to fill the headspace. This achieved a gas sample with high purity.

When reference data was taken, the sample flask was attached to the absorption cell via an electronic valve. The cell and piping through the valve were evacuated to a low pressure to remove any remaining gas from the cell and the connecting sample flask. Once a good vacuum was achieved, the cell was closed off from the vacuum pump, the electronic valve was closed, and the flask was opened so that the pure gas could fill the pipe up to the valve. The valve was then briefly pulsed to allow a controlled volume of

gas to fill the cell to a desired pressure. Generally, this was around 1 mTorr. For some strongly absorbing gases, the gas began to power saturate. To overcome this, lab air was pulsed into the cell until pressure in the cell was high enough for collisions to thermalize the rotational populations.

With the gas loaded, a wide sweep of the full spectral range was performed in order to identify rotational lines with the largest amplitude. This was repeated with each of the pure gases so that potential overlaps could be avoided when selecting specific lines for the library. To ensure rapid acquisition times and moderate redundancy, three lines for each compound were chosen for use as the reference library and future data collection. Once the lines had been chosen, the cell was filled again, and frequency snippets centered on the selected lines were probed. The recorded spectrum was averaged extensively to ensure the library spectrum had minimal noise.

After reference spectra for all the selected compounds were collected, each was normalized for use on any system. Raw spectral data was corrected for nonlinear effects of the receiver diode. The diode compressed the absorption lines and broke the linear relation of gas pressure and amplitude. Correcting for this compression was necessary for library fitting. Pressures for each compound were assigned to each library spectrum. A set of three snippets were selected based on their strength in the sensor. Each set of spectral snippets was scaled by the corresponding gas pressure, equipment gains, path length, and the baseline power such that the library represented the signal of 1 mTorr absorption in a 1 m absorption cell with a baseline of zero and no gain. The scaled libraries were then valid for use in equation 18 to measure an unknown sample.

4. Sensor Characterization

The sensor was characterized by studying the propagation of radiation through the absorption cell and the efficiency of the preconcentration process. The results of this characterization were used to optimize the sensor for robust data acquisition. Due to the coiled cell, the linearly polarized radiation from the source was distorted as it propagated through the cell. The receiver, also linearly polarized, measured maximum signal when aligned with the incoming polarization. Distortion of the polarization was frequency dependent and caused poor transmission at certain frequencies. Optimal orientation was determined by adjusting the angle of polarization of the source and receiver independently to achieve maximal receiver power through a range of frequencies adequate for the detection of rotational lines selected for sensing. Preconcentration parameters were studied by sampling a prepared reference gas mixture with known concentrations of the constituent gases. This data was also used to determine benchmark values for detection of the compounds studied.

4.1 Source-Receiver Orientation Optimization

To ensure the spectra recovered had optimal signal to noise, the power transmitted through the cell was probed with the source and receiver in several orientations. As the THz source and receiver had linearly polarized outputs and inputs respectively, the orientation of the source and receiver had a significant impact on the collected signal. Ideally, the maximal signal at the receiver would have been when both source and

receiver were oriented such that the polarization of both are aligned, however due to reflections inside the absorption cell, the polarization of the electric field propagating through the cell was distorted at various input frequencies. To study the impact of the changing polarization, the source and receiver were independently rotated, and the transmitted power was recorded. This was done by recording data in four configurations; source and receiver vertical, source vertical and receiver horizontal, source horizontal and receiver vertical, and source and receiver vertical. Transmitted power in a frequency region from 240-280 GHz was recorded for each of the four orientations. The optimal configuration was chosen when the power transmitted through the cell was greatest and spanned a wide enough range of frequencies to enable selection of rotational transitions in that range.

From these four configurations, a scheme to potentially identify the most optimal source and receiver orientations was developed. An interpolating function was created to attempt to predict the power for source and receiver orientations between the four orthogonal positions recorded. Collected power regions of the four orientations were weighted by the angle of the source and receiver relative to their vertical position to interpolate all orientation angles for the source and receiver. This interpolant had the form:

$$\hat{P}(f,\theta_S,\theta_R) = \left[cos(\theta_S)cos(\theta_R)e^{i\theta_1}\sqrt{p(f,0,0)} + cos(\theta_S)sin(\theta_R)e^{i\theta_2}\sqrt{p\left(f,0,\frac{\pi}{2}\right)} + sin(\theta_S)cos(\theta_R)e^{i\theta_3}\sqrt{p\left(f,\frac{\pi}{2},0\right)} + sin(\theta_S)sin(\theta_R)e^{i\theta_4}\sqrt{p\left(f,\frac{\pi}{2},\frac{\pi}{2}\right)}\right]^2 \qquad (equ.\,19)$$

where $\hat{P}$ = the interpolated power for a given frequency and source receiver orientation

f = the frequency of the input radiation

θ_S = the angle of the source relative to vertical

θ_R = the angle of the receiver relative to vertical

θ_{1-4} = the phase of the electric field for each orientation

p = the measured power for a specific frequency and orientation, f, θ_S, and θ_R

Interpolation in this form attempted to match the angular dependence and phase of the electric field of the radiation in the cell. The sine and cosine factors in each term ensured that the function would return the experimentally measured power when the input orientation matched one of the four corresponding basis orientations. By adjusting the orientation of the source and receiver and accounting for field phase, the transmitted power was predicted and optimized.

4.2 Preconcentration Assessment

Preconcentration processes of the sensor were assessed to determine the optimal procedure and parameters to maximize sensor sensitivity. The adsorption process of the thermal desorption tubes did not guarantee that all the compounds of interest are trapped in and desorbed from a sorbent tube. Some gas could break through the sorbent material and be removed with the background gases. Gas loss introduced a difference between the spectroscopically measured partial pressure in the absorption cell and the true partial pressure of the gas in the sample. The ratio of the spectroscopically determined pressure to the true partial pressure was called the preconcentration efficiency of the sample process. Accounting for this efficiency was necessary in order to have an accurate quantitative measure of the true gas concentration in the sample. As such, preconcentration efficiency was the primary focus to ensure as much of the compounds

of interest in the sample were delivered to the absorption cell for analysis. This ensured that the minimum detectable concentration in the atmospherics sample was as small as possible.

4.2.1 Reference Mixture Preparation

Preconcentration efficiency of the sensor was characterized for a variety of preconcentration parameters. Sample volume, flow rate, trapping temperature and desorption temperature were each varied in order to determine the optimum set to achieve the best preconcentration efficiency across selected compounds. For this purpose; acetaldehyde, acetone, ethanol, formaldehyde, and isoprene were chosen to evaluate their respective preconcentration efficiencies. These three lighter, volatile species; acetaldehyde, ethanol, and formaldehyde and two less volatile, moderate weight molecules, acetone, and isoprene represented a range of volatility and rotational absorption sensitivity. A reference gas sample consisting of these gases, water vapor, and nitrogen was prepared. The spectroscopically determined concentration from the sensor was then compared to the known concentration of the reference to determine the preconcentration efficiency. Each parameter was independently varied from a central set. The effect of each parameter on efficiency was assumed to be separable over the range of values tested. Independence of the parameters was determined from preliminary testing. This central parameter set had a sample volume of 0.5 L, a flow rate of 0.2 L/m, a trapping temperature of 15 C and a desorption temperature of 140 C. Two additional measurement for each parameter were made with the parameter studied either increased or decreased slightly while all others were held to the central set.

To facilitate the preconcentration efficiency assessment, a reference gas mixture with known concentrations was created. Preparation of the reference mixture was done by taking high purity, spectroscopic grade liquid samples of the five compounds and diluting each in 52 ml of distilled water with the exception of isoprene. Isoprene is not solved in water and therefore would not dilute properly. For each compound, 0.05 ml was drawn in a 0.5 ml syringe and added to the volume of distilled water. A pure sample of formaldehyde was not available, instead a 37% by weight solution of formaldehyde in water with 10-15% methanol as a stabilizer to prevent polymerization was further diluted in the 52 ml of water [45]. The addition of the methanol stabilizer provided an opportunity for an estimate of methanol preconcentration efficiency. A small volume,

Table 1 Prepared Reference Mixture

Compound	Initial Volume (µl)	Water Dilution (ppm)	Gas Dilution (ppm)
Acetaldehyde	50 ± 5	307 ± 31	2.31 ± 0.33
Acetone	50 ± 5	233 ± 23	1.75 ± 0.25
Ethanol	50 ± 5	296 ± 30	2.22 ± 0.31
Formaldehyde	20 ± 1	191 ± 6	1.43 ± 0.15
Methanol	7 ± 1	060 ± 12	0.45 ± 0.10
Isoprene	0.5 ± 0.1		13.56 ± 2.71

Tab. 1 Volumes of the diluted pure compounds, the combined volumetric dilution in water, and the final volumetric dilution in the tedlar bag containing 9 L of dry nitrogen. Isoprene was not solvable in water. Instead of diluting isoprene in the water, a small sample was injected directly into the tedlar bag with a µl syringe.

0.05 ml, of the diluted mixture was drawn with a 0.5 ml syringe and injected in to a 10 L tedlar gas sampling bag [46] filled with 9 L of dry, ultra-high purity (UHP) nitrogen. Isoprene, due to lack of solubility in water, was injected directly into the bag using a 0.5 µl syringe.

Between each syringe injection the puncture in the bag was sealed with plastic tape. Once all compounds were injected into the gas bag, the gaseous dilution of each of the compounds was around 1 ppm with the exception of isoprene which was near 10 ppm.

The initial volume in microliters (µl) and subsequent dilutions, parts per million (ppm), for the dilution in water and in gas of each compound are shown in table 1. Formaldehyde and methanol volumes have been calculated from a 0.05 ml volume of the solution. Isoprene has a much weaker rotational spectrum compared to the other selected compounds, so a larger concentration was needed to ensure robust spectra. The tedlar bag

Table 2 Prepared 'Direct Injection' and Dilute Reference Mixtures

Compound	Initial Volume (µl)	Direct Injection / High Concentration Gas (ppm)	Dilute Mixture / Low Concentration Gas (ppm)
Acetaldehyde	1.00 ± 0.14	54 ± 8	0.067 ± 0.009
Acetone	20 ± 5	800 ± 200	1.0 ± 0.3
Ethanol	10 ± 5	500 ± 300	0.6 ± 0.3
Methanol	2.08 ± 0.20	156 ± 10	0.195 ± 0.019
Isoprene	400 ± 5	12,100 ± 200	15.1 ± 0.2

Tab. 2 Volumes of the pure compounds injected directly in to a tedlar bag containing 8 L of dry nitrogen. From the direct injection / high concentration gaseous mixture, 10 ml were drawn and injected into another tedlar bag filled with 8 L dry nitrogen to dilute the mixture to levels suitable for preconcentration.

was left to rest overnight which allowed the reference mixture to equilibrate. This ensured an equal distribution of gas throughout the bag before sampling. Prior to sampling the bag was heated with a lamp for at least 10 min to promote any condensed compounds back into the gas phase.

4.2.2 'Direct Injection' Mixture Preparation

An alternative method of preconcentration efficiency assessment was performed to attempt to reduce the uncertainty in the prepared gas mixture. Another reference gas mixture was prepared using the same spectroscopic grade liquid compounds. Rather than dilute in water, a larger volume of pure sample was drawn with a syringe and injected directly into a 10 L tedlar bag filled with 8 L of dry UHP nitrogen. Gaseous concentrations were targeted such that they would be just above the expected minimum

spectroscopic detectable level in the cell. The injected volume and final concentration are shown in Table 2. A 0.5 ml syringe was used to load liquid samples for acetone, ethanol, and isoprene. The remaining chemicals were added using a 0.5 µl syringe. To achieve initial volumes greater than 0.5 µl, several draws of the syringe were used.

This sample was then left to equilibrate overnight. Once the gas had rested, the bag was heated with a lamp to minimize condensation and 10 ml of gas was drawn from the mixture. The drawn 10 ml was injected into a 10 L tedlar bag with 8 L of dry UHP nitrogen. This produced a dilute mixture suitable for preconcentration. The source ‘direct injection’ bag was then attached to the absorption cell bypassing the preconcentration unit. A volume of gas was pulsed to fill the cell where the MKS pressure gauge read about 46 mTorr. Prior to filling the cell, the bag was heated with a lamp again. Spectra of the five compounds were recorded and used to determine the concentration of the high concentration mixture. This enabled a spectroscopically accurate assessment of the gas mixture to avoid uncertainty in the liquid volume measurements. The diluted low concentration mixture was then processed with preconcentration at three temperatures. The resulting concentrations could then be compared to the spectroscopically determined concentration of the high concentration bag. The ratio of the two concentrations, once corrected for the volumetric dilution of 10 ml into 8 L, indicated the preconcentration efficiency of the sensor.

5. Results

5.1 Optimal Source-Receiver Orientation

To characterize the transmission of power through the 7.8 m coiled cell. Power was measured with the source and receiver in four orthogonal orientations: source and receiver vertical; source vertical, receiver horizontal; source horizontal, receiver vertical; and source and receiver horizontal, were measured. The power for each orientation is shown in figure 2. These four orientations were used to select the optimal orientation for future data collection. Transmitted power was largest when the source and receiver were both in the vertical orientation. This orientation had several regions with low power, significantly, the power nearly went to zero near 255, 265, and 278 GHz. The precise nature of the interference which caused these low power regions was unclear. Other orientations had peak power around half that of the 'vertical-vertical' orientation but were able to transmit some power in some of the missing frequency regions.

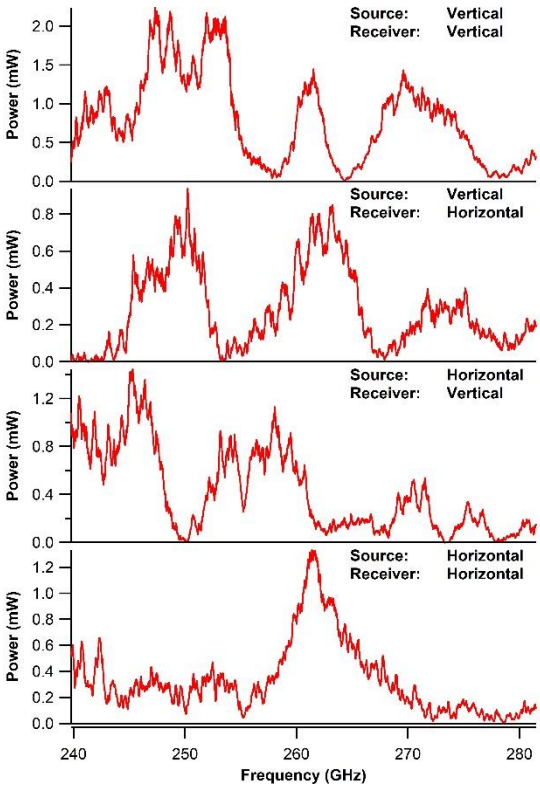

Fig. 2 Power transmitted through the absorption cell for each orthogonal, source-receiver orientation.

Comparing the four orientations, each had regions of near zero power which would make measurement of spectral lines in that region a challenge. As the ‘vertical-vertical’ orientation had the largest transmitted power, it was selected as the best orientation. Regions of higher power, in this orientation, were wide enough to accommodate many rotational lines for detection. Additionally, low power regions were narrow enough to enable some noisier detection outside the regions of strong transmitted power. Combined, these reasons made the ‘vertical-vertical’ orientation the best choice for spectral measurements.

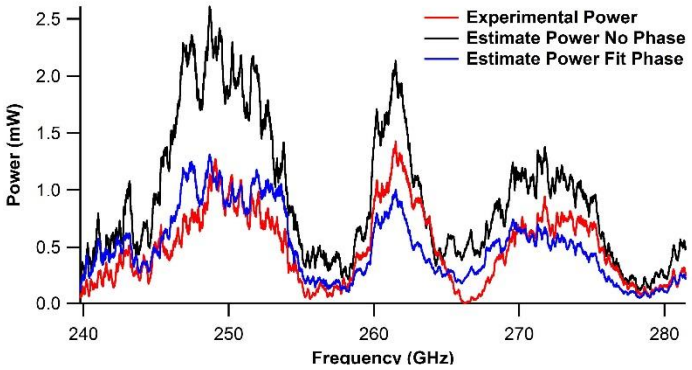

Fig. 3 Measured transmitted power (red) for the source oriented at 0° from vertical and receiver oriented at 45° from vertical compared the estimated power from interpolant function, equ. 19, with matching source and receiver angles all phases fixed to zero (black) and the estimated power with phase determined from fit to the experimental data (blue).

The interpolation function was tested for validity using these four measured orientations as a basis for interpolation. The source was left in the vertical position and the receiver was rotated to 45° from the vertical. This configuration produced an interpolant that was equal parts the power from the ‘vertical-vertical’ orientation and the ‘vertical-horizontal’ orientation. Power was collected from 240-280 GHz to match the range of the interpolant basis data in the interpolant. Angles of the source and receiver were input into the interpolant while the phase of each basis was held to zero. This generated estimated transmitted power data. The experimental and zero phase interpolated data were then

compared to inspect the performance of the interpolant as a method to predict optimal orientation. The two data sets are shown as red and black traces respectively in figure 3.

The estimate power of the zero-phase interpolant did a reasonable job of predicting the general trend of the experimental data, although it did overestimate the power. Unfortunately, the regions of zero power that were predicted to increase by the interpolant remained near zero in experimental data. The lack of improvement in these low power regions likely came from the phase of the transmitted radiation, which could have destructively interfered with itself and caused the lower power. The prediction of optimal orientation could have been improved by incorporation of the phase into the interpolant.

To incorporate phase, an estimate was determined by fitting the interpolant to the experimental 0° source angle, 45° receiver angle data with the orientation angle fixed and leaving the θ_2 free. The remaining phases; θ_1, θ_3, and θ_4, were held to zero as only θ_1 and θ_2 contributed to the interpolant in the orientation and only difference between the two phases impacted the final estimation. This fit phase was used to generate another interpolant also shown as the blue trace in figure 3. The final interpolant showed a better match to the experimental data than the zero-phase estimate in terms of amplitude. The residual discrepancy was likely due to the assumption that the phase was constant throughout the frequency range.

The wide frequency sweeps collected for the orientation assessment demonstrated standing wave patterns from a variety of sources. One such cavity source was likely the ends of absorption cell itself which created a standing wave from reflections off the source and receiver. Periodicity of this standing wave contained information about the effective cavity length of radiation in the cell. As the cell was a complicated coil, determining the path length of the radiation inside the cell was a challenge. Assessing the path length from the standing wave was the best possible method for an accurate determination.

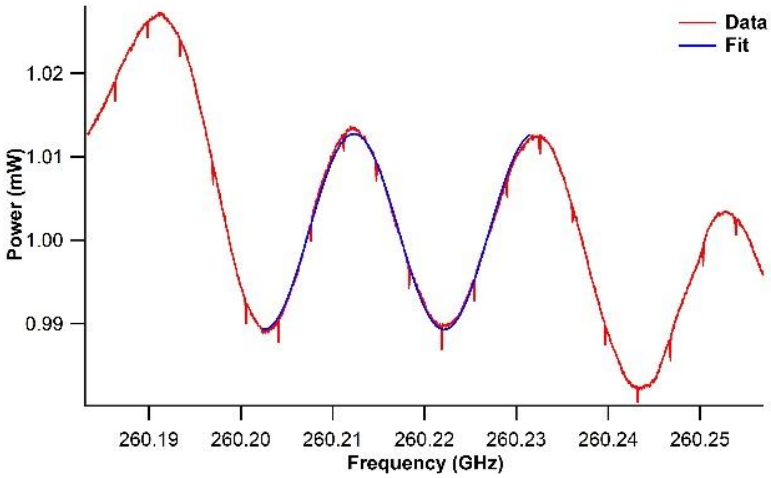

Fig. 4 Standing wave pattern in the source-receiver vertical orientation (red) and the offset sinusoidal fit (blue) used to determine the FSR of absorption cell.

A fit to these standing was used to determine the free spectral range (FSR) of the effective cavity and its length. A vertically offset sinusoidal wave was fit to a small region of the standing wave pattern in order to determine the FSR. This is shown in figure 4. The ticks seen on the data were artifacts of the receiver. The underlying power curve of the detector and the mixing of other standing wave patterns made finding a large number of oscillations difficult. However, the fit matched well over the chosen one and a half oscillations, which gave confidence to the quality of the derived effective path length. The fit FSR was found to be 320.1 ± 0.3 GHz which corresponded to an effective

path length of 7.636 ± 0.007 m. This was a reasonable path considering the tube length used to create the coil was 7.8 m.

5.2 Library Development

Library spectra were taken for each compound of interest. This was done by pulsing the electronic inlet valve to let pure gas into the absorption cell until a target pressure was reached. This pressure was generally around between 0.1 to 1 mTorr. For strongly absorbing gases, power saturation began to occur at the targeted pressures. The effect of

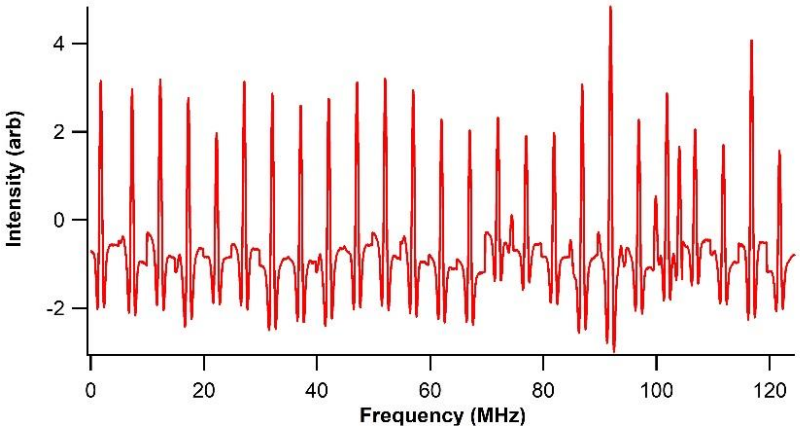

Fig. 5 Selected snippets of ethanol for library generation. The horizontal axis shows the frequency spanned by all the snippets. Each line is centered about its transition frequency and is not continuous with its neighbors. 32 passes of the 2nd harmonic demodulated spectral lines were averaged to minimize noise.

power saturation was reduced by pulsing pure gas to a desired pressure and then pulsing lab air into the cell to ensure the collisional rate in the cell was high enough to thermalize the gas and prevent power saturation. For each compound, a broad overview spectrum was taken to identify strong lines in regions with reasonable power in the range of the source. About 20 strong lines for each compound were selected for frequency snippets. The cell was filled again, and the snippets were recorded with a large number of averages to minimize noise. An example of this snippet spectrum for ethanol is shown in figure 5.

A pressure was assigned to the snippet spectrum and three of the strongest lines were selected to serve as the new library. The lines were scaled by the assigned pressure, the associated gains, and the path length of the radiation in the cell determined from the fit to the free spectral range. The snippets also were scaled by their corresponding baseline power and subtracted to remove the baseline. Scaling of the snippets produced libraries scaled to unit gain and path length with a zero-power baseline and a library pressure of 1 mTorr. These libraries were then valid for use in any system.

5.3 Preconcentration Parameter Selection

5.3.1 Optimal Parameters

From the 12 preconcentration cycles, three for each of the four parameters evaluated, of the reference mixture, parameter dependent efficiencies were determined. These efficiencies were determined by the ratio of the experimentally measured concentration to the predicted concentration of the reference mixture given in table 1. Determined efficiencies are shown in figure 6. Formaldehyde was removed from consideration due to contamination issues. Formaldehyde concentrations were near equal with expected reference mixture concentration causing preconcentration efficiencies near or greater than 100%. While 100% would have been ideal, it was not possible due to sample losses from the gas transport in the sensor. As gas was loaded into the sorbent tube, some gas was left in the headspace of the inlet and was not be exposed to the tube. Unaccounted for sample meant the peak efficiency for any gas must be less than 100%. This along with the cycles where formaldehyde efficiency was greater than 100% suggested that there was unknown source of formaldehyde. It was unclear where the contamination came from. It may have been a product of sorbent material outgassing or degradation. It was also possible that it

came from the tedlar bags themselves. Rather than determining the contamination contribution, focus was shifted to an assessment of methanol based on its concentration in the formaldehyde solution.

For each of the four preconcentration parameters tested, trapping temperature, sampled volume, flow rate, and desorption temperature, the resultant efficiencies generally followed expectations across the parameter range with the exception of trapping temperature. For each parameter varied, the remain three were held to a central parameter set; 15 C trapping temperature, 0.5 L sampled volume, 0.2 L/min flow rate, and 140 C

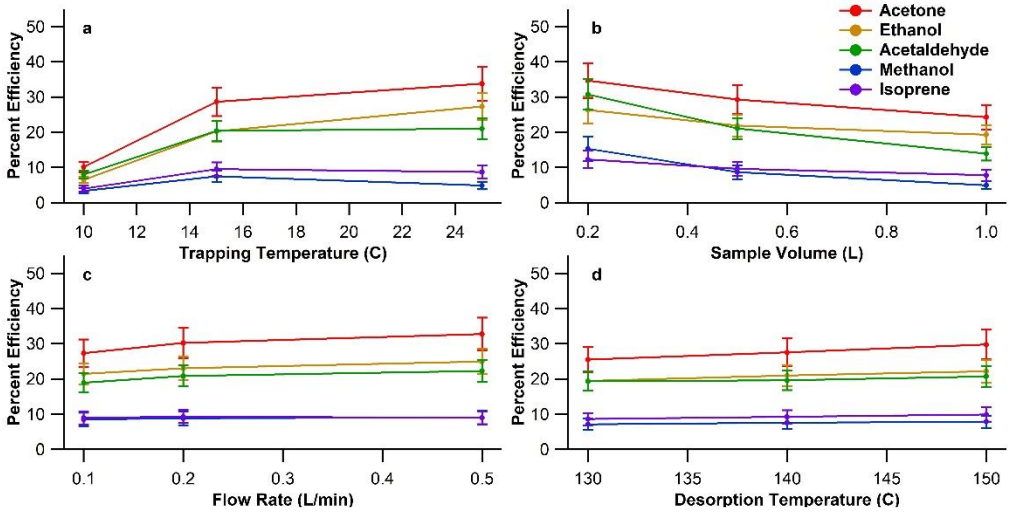

Fig. 6 Calculated preconcentration efficiencies with errors from library fit for the five target compounds; acetone (red), ethanol (yellow), acetaldehyde (green), methanol (blue), and isoprene (purple), over a range of four probed preconcentration parameters: a, trapping temperature; b, sample volume; c, flow rate; and d, desorption temperature, sampled from a common reference mixture. Each triplet of measurements for a given parameter was taken with remaining parameters held. The default parameter set was 15 C trapping temperature, 0.5 L sampled volume, 0.2 L/min flow rate, and 140 C desorption. Each measurement triplet has one measurement taken with this default set.

desorption temperature. Preconcentration efficiencies for each of these measurements are shown in figure 6.

For cycles with varied trapping temperature, (Fig 6 – a), were taken at sorbent tube temperatures, 10, 15, and 25 C. The preconcentration efficiencies did not demonstrate the expected behavior. At lower temperatures, the gas was expected to more readily condense or adsorb onto the sorbent material and be trapped. Low temperature efficiencies showed the opposite result as they were much lower than the other higher temperatures. Preconcentration efficiency was fairly consistent between 15 and 25 C but increased slightly at 25 C for some compounds. This increase, however, was still within the error of each efficiency and was inconclusive.

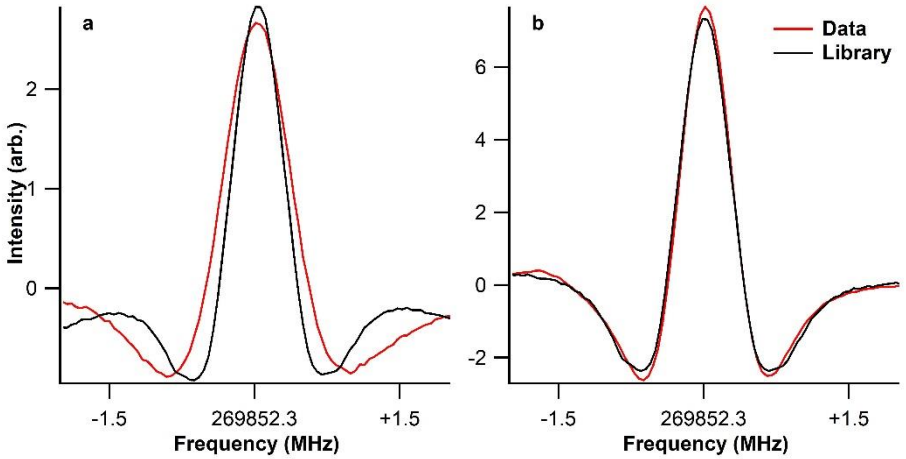

Fig. 7 Comparison of an acetaldehyde absorption line and library fit for pressure broadened samples. The sample trapped at 10 C, a, shows the widening of the line and the reduction in peak amplitude in the experimental data (red) compared to the library fit (black). The sample trapped at 25 C, b, shows the better match between the data and library in the unbroadened data.

It was determined that the unexpectedly low efficiency at 10 C was due to excessive retention of water vapor during preconcentration and consequent higher pressure broadening of spectral lines. The mixture was prepared by injecting 0.05 ml of dilute samples into 8 L of gas. As the pure samples were fairly dilute, this meant that a large portion of the liquid was water. The large water content caused the sample humidity to be near 100%. When the gas sample passed through the cooled preconcentration unit, water readily condensed on the sorbent material at 10 C. This water was retained rather than

removed by the headspace evacuation. Water vapor delivered to the cell caused the pressure in the cell to increase beyond Doppler limitations and broadened the absorption lines used to determine the partial pressure in the cell. This broadening caused the peak absorption to drop and the line width to widen, the library fit, lacking that broader line shape, underestimated the pressure in the cell. The effect of the fit to a broadened line can be seen in figure 7 which compares an experimental absorption line of acetaldehyde to the library fit for a sample trapped at 10 C and 25 C. This caused the reported pressures to be lower than reality and the preconcentration efficiency to be underestimated. In reality, the absorption line still contained all the pressure information for the compound, but some of that information was lost from the peak intensity to the width of the line and was not recovered in the library fit. The low temperature preconcentration was likely similar or even better than the cycles at higher temperatures as was expected but the linear library fit was not be able to determine it. Due to this limitation, temperatures lower than 15 C gave inconsistent results and so the typical preconcentration temperature was kept at 15 C.

For the cycles where sample volume was varied (Fig 6 – b), the reference mixture was sampled with a volume of 0.2, 0.5, or 1 L. The determined efficiency for these volumes was not greatly changed within the error. There was a slight downward trend with increasing sampling volume which was expected as the sorbent tubes became more saturated with compounds. It was unclear if this trend demonstrated real saturation of the sorbent tubes or was coincidence.

Selection of optimal sample volume depended on several operational factors as well as the preconcentration efficiency. Larger sample volumes would deliver higher sample

pressures until the sorbent tubes saturated. Higher sample pressures in the cell would increase the absorption signal for a given atmospheric sample and would result in lower detection thresholds. Gain in sensitivity from the lower detection threshold needed to be balanced against the total sampling time, as a larger sample would require more time to draw through the cell and would consume the source gas more rapidly.

Based on the three sample volumes, there did not seem to be significant saturation of the tubes. The gain in preconcentration efficiency at lower volumes was not significant while the potential reduction in detection threshold with 0.2L was more significant when compared to the 0.5L, a factor of two and a half reduction, and to the 1L volume, a factor of five reduction. Between the 0.5L and 1L volume, there was a factor of two reduction in detection threshold but also a factor of two increase in the gas consumed and draw time. This increase in gas consumption reduced the opportunity for redundant measurements as the sample was depleted more rapidly. With consideration of each of these effects, 0.5L was chosen as the ideal operational sample volume to balance the detection threshold vs sampling time and redundancy.

The preconcentration cycles where flow rate was varied, (Fig 6 – c), were largely consistent with our expectations. Three measurements sampled the gas with flow rates set by the flow mass controller at 0.1, 0.2, and 0.5 L/min. It was expected that flow rate should have a minimal effect on the trapping of samples in the sorbent tubes. However, at high flow rates there was an increased risk of sample traveling though the sorbent material without being trapped. From the determined efficiencies, this did not seem to occur.

There was a slight positive trend in the preconcentration efficiency with the sample rate. This was likely not real as all values were nearly the same within error. As the flow did not seem to impact the preconcentration efficiency there was no apparent optimal flow rate. The rate was chosen arbitrarily and selected to be as large as possible to minimize the sampling time. A limit to the flow rate came from the stability of the flow mass controller. The OMEGA FMA-6500 controller was specified for 0.01 to 0.5 L/min. Flow rates near the bounds or outside the specified range caused the flow rate to oscillate rather than reach a steady state flow. The oscillation caused issues in tracking the total volume sampled due to the swings in flow rate. To avoid this instability, flow rates were generally kept at or below 0.4 L/m.

Desorption temperature was studied in three preconcentration cycles with set temperatures; 130, 140, and 150 C, (Fig 6 – d). Efficiencies determined from these samples were also near constant within the measured error. There did appear to be a slight trend of increasing efficiency with increasing temperature. If real, this trend was consistent with expectations. When desorbing, some gas remained trapped in the material at the lower temperature and was not accounted for spectroscopically. Increased temperature was able to cause the material to release more of the trapped gas.

Optimal desorption temperature depended on the temperature where the most sample was released for analysis while damage to the sorbent material was minimized. At higher temperatures, the risk of damage to the sorbent tube was increased. This also decreased the lifetime of the sorbent tube before it needed to be replaced. As the measured preconcentration efficiencies did not vary greatly over the tested temperature range, there was likely not much risk of losing a significant amount sample due to lack of desorption.

Higher temperatures could have been probed to assess what additional efficiency could have been gained but was not pursued do to the increased risk of permanent damage or destruction of the sorbent. For this reason, and the insignificant efficiency increase at 150 C, desorption temperatures were kept to 140 C out of caution.

5.3.2 Sample Repeatability

Having considered each of the four parameters, the performance of the preconcentration system was reasonably well characterized. Each calculated efficiency was determined from a single measurement due to limited sample availability, increasing the associated uncertainty. Repeatability of measurements was assessed from this dataset by considering the cycles with parameters in the central set. For each of the four parameters, there was a cycle where 0.5 L was sampled at 0.1 L/min, trapped at 15 C, and desorbed at 140 C. Figure 8 shows the pressure in the cell for these four sets of data. Error bars matching the color of the point were determined by the error of the library fit and did not reflect preconcentration variance. The black error bars are the standard deviation of the four measurements for each chemical. While each chemical did vary more than the error from the fit residuals, the overall standard deviation was only a few percent of the

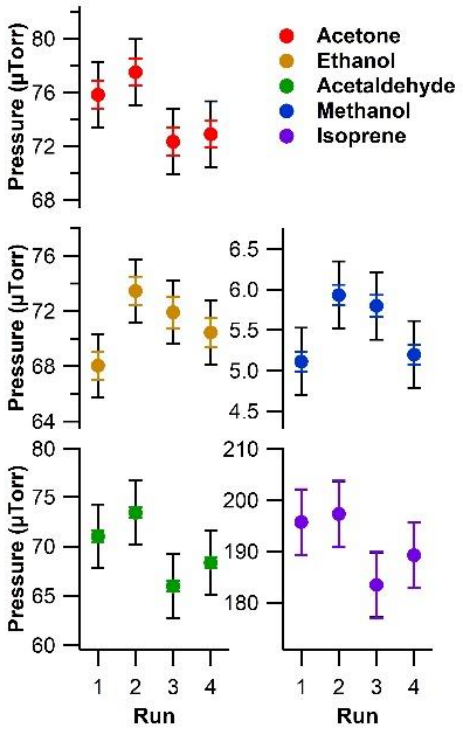

Fig. 8 Demonstration of repeated sampling from common mixture. The fit pressure and fit error for the default parameter cycle of each measurement triplet is shown for; acetone (red), ethanol (yellow), acetaldehyde (green), methanol (blue), isoprene (purple). The standard deviation of the four measurements in shown as black error bars on each point.

absolute pressure. This indicated that the preconcentration process under the sampled conditions was reasonably consistent between repeated samples.

5.3.3 Direct Injection Mixture Assessment

Based on the data of the 12 preconcentration cycles, the preconcentration efficiencies were determined in comparison to a prepared reference mixture. This mixture was a potential source of much of the error in the determined efficiencies as the preparation of small samples of each pure chemical were challenging. Additionally, once prepared in the tedlar bag, the true gas phase concentration was not known, as condensation on the walls could occur. The heating of the bag prior to and during the sampling should have reduced the effect of condensation. However, if not all of the compound was driven into the gas phase then the sampled concentration would be lower than expected and the preconcentration efficiency would appear to be lower than reality. To overcome this uncertainty, two reference gas mixtures were prepared such that one was derived from the other. The concentration of the source mixture was then spectroscopically determined to attempt to provide a more accurate estimate of the true gas concentration rather than rely on precise knowledge of the prepared volumes of pure compound. This source mixture was then diluted to produce gas concentrations suitable for preconcentration.

Table 3 Measured Values of Direct Injection and Dilute Mixtures and Ratio to Predicted Values

Compound	Direct Injection (ppm)	Dilute Mixture (ppm)	Predicted to Measured Ratio
Acetaldehyde	7 ± 3	0.009 ± 0.005	7.24
Acetone	188 ± 20	0.235 ± 0.020	4.34
Ethanol	207 ± 20	0.258 ± 0.030	2.51
Methanol	19 ± 7	0.024 ± 0.009	8.08
Isoprene	5,760 ± 846	7.191 ± 1.000	2.10

Tab. 3 Measured concentrations of the 'direct injection' and 'dilute' mixtures and a ratio of the predicted concentrations from table 2 to the measured values. 'Direct injection' concentrations were determined from library fits to the gas sample bypassing preconcentration. The 'dilute' concentrations are derived from these measurements and were scaled by the volumetric dilution.

The high concentration, source mixture was prepared by injecting a volume of pure compound, volumes are given in table 2, directly into 8 L of dry nitrogen. The 'direct injection' mixture was delivered directly to the absorption cell bypassing the preconcentration unit. An electronic valve pulsed the reference gas into the cell until 46 mTorr of the mixture filled the cell. Rotational spectra were recorded for each compound of interest and the absorption lines were fitted to determine the partial pressure of the gas in the cell. It was assumed that the partial pressure in the cell would be representative of the partial pressures in the source mixture. From the 'direct injection' mixture, 10 ml of gas was added to another bag with 8 L of dry nitrogen to dilute the high concentration of gases. The concentrations of the diluted mixture are given in table 2. After dilution, the gases were no longer in danger of saturating the sorbent tubes. This dilute mixture was processed with preconcentration at three trapping temperatures; 10, 15, and 25 C, each was a 0.5 L sample flown at a rate of 0.2 L/min and desorbed at 140 C. The resulting concentrations were determined from library fits to the preconcentrated sample. Partial pressures from the high concentration sample were used to determine the concentration of each compound in the sample. This was then scaled by the dilution factor to get the concentration of the low concentration sample. Concentrations from each sample are

shown in table 3 along with the ratio of the predicted concentrations from table 2 to the measured dilute mixture.

The ratios of predicted spectroscopically measured concentration of the ‘direct injection’ mixture showed a significant discrepancy. The large ratios suggest that there were some sample losses either when preparing the ‘direct injection’ mixture or when delivering the gas to the absorption cell when the preconcentration system was bypassed. A possible cause of this discrepancy was the incomplete delivery of the liquid compound to the tedlar bag. As the injected volumes of each compound were generally small, surface tension caused the liquid to bead on the syringe. Care was taken to ensure this bead was released into the bag but if it had failed to detach, the concentration of the gas in the mixture was underestimated. This issue highlighted one of the reasons direct knowledge of the gas concentration separate from the mixture preparations was needed to ensure a robust estimate of preconcentration efficiency.

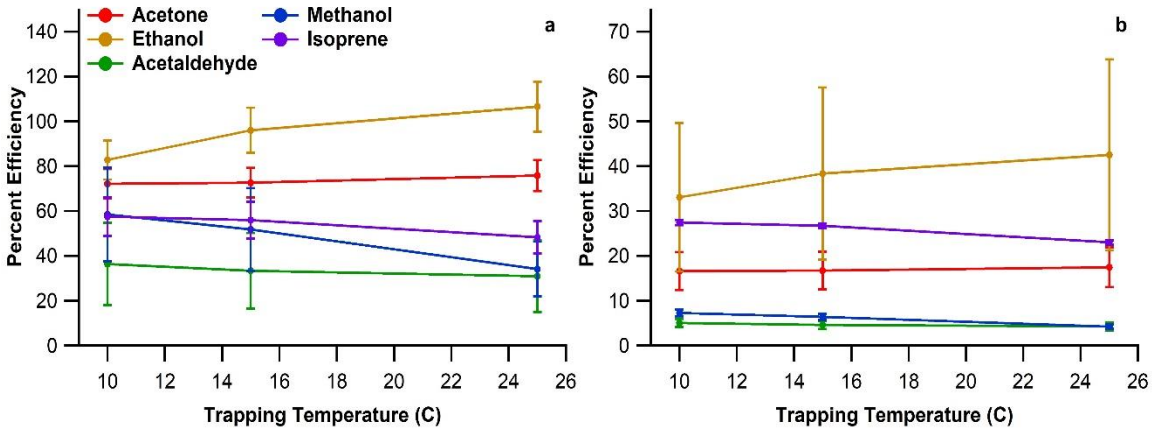

Fig. 9 Calculated preconcentration efficiency for; acetone (red), ethanol (yellow), acetaldehyde (green), methanol (blue), isoprene (purple). (a) Efficiencies are determined from the ratio of the measured dilute mixture to the spectroscopically measured ‘direct injection’ mixture. Errors are derived from the residual in the fits. (b) Efficiencies calculated from the ratio of the measured dilute mixture to the predicted concentrations determined from the preparation of the ‘direct injection’ mixture. Errors are derived from errors in the injected volumes of the prepared mixture and the residuals in the fit.

By comparing the low concentration data with the results from the three preconcentration cycles, preconcentration efficiencies were calculated. These are shown in figure (9-a) for

each compound at the three trapping temperatures. Under this reference scheme the preconcentration efficiency of each gas had increase dramatically, along with the associated errors. A promising sign was the lack of a sharp drop in efficiency at 10 C which demonstrated a reduction of water vapor in the mixture. Surprisingly, the efficiency did not increase much at this lower temperature. Methanol efficiency did improve with decreased temperature which may be due to its higher volatility. Ethanol still showed a decrease in efficiency at lower temperatures. Efficiencies for each compound were still within the error from one another and the variation could have been due to preconcentration variance. The large error came from the fit error to the direct injection where most compounds were nearing their detection threshold. This lowered the signal to noise and increased the residuals of the fit.

The increased efficiencies caused some concern as the preconcentration efficiency of ethanol was above 100% at 25 C which was not possible. This suggested that there was some significant error in the comparison of the two mixtures. As a comparison to the previous preconcentration assessment, the efficiencies were also calculated using the measured concentrations of the dilute mixture and the predicted concentrations from the ‘direct injection’ mixture preparation. Errors for these efficiencies were derived from the fit error in the measured concentrations and the error in the initial volumes used in sample preparation. Figure (9-b) shows these new efficiencies and errors. As the volumes delivered were small compared to the available syringes, the error was dominated by the uncertainty in sample preparation. This error was anticipated but was expected to be irrelevant once the ‘direct injection’ mixture had been spectroscopically quantified.

Between the new efficiencies and those determined from the first reference mixture, the general order of efficiency was preserved, with exception of acetaldehyde which was reduced and isoprene which was increased. Based on this similarity, it was assumed that the source of the discrepancy between the two sets of preconcentration efficiencies stemmed from issues with the measurement of the direct injection mixture which caused it to be underestimated. This was likely caused by the warmed gas condensing onto the walls of the piping that bypassed the preconcentration system. The condensation resulted in a deficit of gas in the cell that was reflected in the pressure fit. Due to this issue, the preconcentration efficiencies from the previous reference mixture have been treated as the most representative measurements. Preparation of the first mixture had more precise estimates of the sample concentration giving greater confidence in the resulting efficiencies.

5.4 Detection Thresholds

Although the preconcentration bypass method ultimately struggled to provide a more accurate assessment of efficiency it did allow data to be taken at cell partial pressures near the detection limit. This lower bound of detection coupled to the preconcentration efficiency from the first reference mixture enabled the minimum detectable concentration in an atmospheric sample to be determined. The low-pressure data and the associated fits are shown with their reported partial pressures in figure 10. Errors shown in figure 10 were derived from residuals from the fit of the library and represent the noise on the weak absorption line.

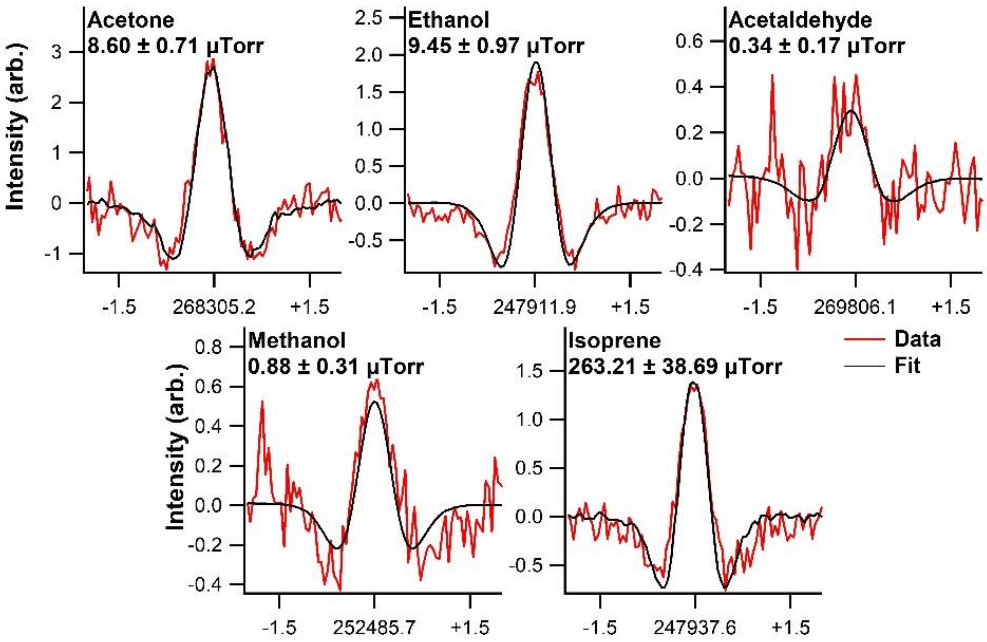

Fig. 10 Noise limited spectra (red) and fits (black) for the five targeted compounds from the direct injection of the high concentration reference mixture into the absorption cell. Assigned pressures and errors were derived from the library fit. These errors represent the noise present on the weak absorption line.

Least squares fitting was capable of fitting weak lines even when their peak amplitude was on the same scale as the noise, but once the signal had dropped below some threshold, the regression would not be able to separate the absorption line from the noise and the fit would be to the noise. Sampled gas below this threshold would have invalid reported pressures. To determine the noise limited pressure threshold, the signal to noise of weak absorption lines were used to estimate minimum detection pressure. The root mean square of the noise on the line was determined along with the strength of the library line. A ratio of library signal to the root mean square was treated as the experimental signal to noise for each compound. This ratio was applied to the low partial pressures from figure 10 to determine an estimate of the minimum detectable pressure in the cell. Minimum detectable pressure was transformed into the expected concentration in a 0.5 L sample and was corrected for the amount of time spent integrating the signal. This produced minimum detection concentrations for one second of integration per point.

Minimum detectable concentration in the cell was divided by the preconcentration efficiency to estimate the minimum concentration in an atmospheric sample. These values are shown in table 4.

Table 4 Detection Thresholds of Target Compounds

Compound	Measured Pressure (μTorr)	Library Signal to Data Noise	Min Detectable Pressure (μTorr)
Acetaldehyde	0.34	3.66	0.09
Acetone	8.60	14.27	0.60
Ethanol	9.45	18.69	0.51
Methanol	0.88	5.46	0.16
Isoprene	263.21	14.91	17.65

Compound	Min Detectable Concentration in Cell (ppb/$\sqrt{Hz}$)	Minimum Detectable Concentration in Sample (ppb/$\sqrt{Hz}$)
Acetaldehyde	0.53	2.67
Acetone	3.44	12.27
Ethanol	2.89	13.73
Methanol	0.92	12.20
Isoprene	100.86	1087.66

Tab. 4 Measured pressures and signal to noise of absorption line data from figure 9. These values were estimate the smallest detectable pressure in the absorption cell and the atmospheric sample without and with consideration of the associated preconcentration efficiency.

Acetaldehyde showed the greatest sensitivity while others like isoprene had higher detection limits. This was likely due to an underestimate of the signal to noise. Acetaldehyde in figure 10 was nearly at the noise level suggesting that the estimate of detection limits by signal to noise were reasonable, while the other compounds were still several times above their noise level. This may have caused an underestimate of their noise limited, signal to noise and produced higher detection thresholds. With the spectroscopic and atmospheric sample detection thresholds determined, the sensor was well characterized and was ready for use within the explored parameter space.

6. Future Work

Preparation of the reference mixture proved to be a significant source of uncertainty in determining the preconcentration efficiency of the sensor across the parameter space. Confidence in the determined efficiencies and optimized parameters would be increased if the experiment was repeated with a more reliable reference gas mixture. Obtaining a larger sample of reference gases with a more precisely known concentration would enable the assessment of the preconcentration efficiency to be validated or better understood. The larger sample would enable redundant measurements for a given parameter which would enable a deeper understanding of the preconcentration variance for a given parameter. Ideally this mixture would be dry to avoid water vapor saturation at lower trapping temperatures and could be input directly into the absorption cell or preconcentration system to minimize potential sources of contamination such as the tedlar bags. Passivation of the gaseous delivery components would also help in this effort to ensure confidence in the delivered sample concentration.

The humid reference mixture demonstrated a weakness of the library method of gas quantification. Development of a method to better account for pressure broadening effects on an absorption feature would enable a more robust assessment of unknown samples from moist conditions. A potential avenue for the inclusion of pressure broadening could be the addition of a new fit parameter which could account for this change in width. This might be accomplished by utilizing a combination of several

reference libraries with similar sample pressures but varied amounts of broadening. Alternatively, a more sophisticated model of frequency modulated line shape is currently being developed to predict the source absorption line parameters from the demodulated data. This model could produce a more general fit to the broadening caused by pressures delivered to the cell.

An instrumentational modification to minimize the retention of water vapor could also improve the reliability of the gas quantification. It was assumed that the pressure broadening seen in the lower trapping temperature data was largely due to excess water vapor in the cell. By selection of more hydrophobic sorbent materials or the addition of another step in preconcentration to selectively remove excess water vapor may improve the robustness of the spectral fits. The major roadblock to such approaches stems from the necessity of polar molecular species for spectral detection [24]–[26]. As water is also polar, many methods may not be selective enough to reduce the water vapor without significant loss in compounds of interest.

References

[1] W. Jia, G. Liang, Z. Jiang, and J. Wang, "Advances in Electronic Nose Development for Application to Agricultural Products," *Food Anal. Methods*, vol. 12, no. 10, pp. 2226–2240, 2019, doi: 10.1007/s12161-019-01552-1.

[2] G. Lagod, S. M. Duda, D. Majerek, A. Szutt, and A. Dolhanczuk-Srodka, "Application of Electronic Nose for Evaluation of Wastewater Treatment Process Effects at Full-Scale WWTP," *PROCESSES*, vol. 7, no. 5, May 2019, doi: 10.3390/pr7050251.

[3] R. Laref, E. Losson, A. Sava, and M. Siadat, "Support Vector Machine Regression for Calibration Transfer between Electronic Noses Dedicated to Air Pollution Monitoring," *SENSORS*, vol. 18, no. 11, Nov. 2018, doi: 10.3390/s18113716.

[4] S. He *et al.*, "A Review on the Use of Impedimetric Sensors for the Inspection of Food Quality," *Int. J. Environ. Res. Public Health*, vol. 17, no. 14, Jul. 2020, doi: 10.3390/ijerph17145220.

[5] M. Naftaly, N. Vieweg, and A. Deninger, "Industrial Applications of Terahertz Sensing: State of Play.," *Sensors (14248220)*, vol. 19, no. 19, p. 4203, Oct. 2019.

[6] S. Kischkel *et al.*, "Breath biomarkers for lung cancer detection and assessment of smoking related effects — confounding variables, influence of normalization and statistical algorithms," *Clin. Chim. Acta*, vol. 411, no. 21, pp. 1637–1644, 2010,

doi: https://doi.org/10.1016/j.cca.2010.06.005.

[7] K. Schmalz, N. Rothbart, P. F.-. Neumaier, J. Borngräber, H. Hübers, and D. Kissinger, “Gas Spectroscopy System for Breath Analysis at mm-wave/THz Using SiGe BiCMOS Circuits,” *IEEE Trans. Microw. Theory Tech.*, vol. 65, no. 5, pp. 1807–1818, 2017, doi: 10.1109/TMTT.2017.2650915.

[8] N. Rothbart, O. Holz, R. Koczulla, K. Schmalz, and H.-W. Hübers, “Analysis of Human Breath by Millimeter-Wave/Terahertz Spectroscopy.,” *Sensors (14248220)*, vol. 19, no. 12, p. 2719, Jun. 2019.

[9] K. M. Dubowski, “Breath Analysis as a Technique in Clinical Chemistry,” *Clin. Chem.*, vol. 20, no. 8, pp. 966 LP – 972, Aug. 1974.

[10] K. Lamote, E. Janssens, E. Schillebeeckx, T. S. Lapperre, B. Y. De Winter, and J. P. van Meerbeeck, “The scent of COVID-19: viral (semi-)volatiles as fast diagnostic biomarkers?,” *J. Breath Res.*, vol. 14, no. 4, p. 42001, 2020, doi: 10.1088/1752-7163/aba105.

[11] P. Gouma, S. Sood, M. Stanacevic, and S. Simon, “Selective Chemosensing and Diagnostic Breathanalyzer,” *Procedia Eng.*, vol. 87, pp. 9–15, 2014, doi: https://doi.org/10.1016/j.proeng.2014.11.254.

[12] R. E. Mather and J. F. J. Todd, “Chemical ionisation mass spectrometry: A survey of instrument technology,” *Int. J. Mass Spectrom. Ion Phys.*, vol. 30, no. 1, pp. 1–37, 1979, doi: https://doi.org/10.1016/0020-7381(79)80040-6.

[13] J. Hodgkinson and R. P. Tatam, “Optical gas sensing: a review,” *Meas. Sci.*

Technol., vol. 24, no. 1, p. 12004, 2012, doi: 10.1088/0957-0233/24/1/012004.

[14] S. Seferaj *et al.*, "Evaluation of a new simple collection device for sampling of microparticles in exhaled breat," *J. Breath Res.*, vol. 12, no. 3, p. 36005, 2018, doi: 10.1088/1752-7163/AAAF24.

[15] R. Sarno, S. I. Sabilla, and D. R. Wijaya, "Electronic Nose for Detecting Multilevel Diabetes using Optimized Deep Neural Network.," *Eng. Lett.*, vol. 28, no. 1, pp. 31–42, Jan. 2020.

[16] B. T. E. Andrews *et al.*, "Measurement of breath acetone in patients referred for an oral glucose tolerance tes," *J. Breath Res.*, vol. 12, no. 3, p. 36015, 2018, doi: 10.1088/1752-7163/AABD88.

[17] B. de Lacy Costello *et al.*, "A review of the volatiles from the healthy human body," *J. Breath Res.*, vol. 8, no. 1, p. 14001, 2014, doi: 10.1088/1752-7155/8/1/014001.

[18] E. Baltussen, C. Cramers, and P. Sandra, "Sorptive sample preparation – a review," *Anal. Bioanal. Chem.*, vol. 373, no. 1, pp. 3–22, 2002, doi: 10.1007/s00216-002-1266-2.

[19] H. MENG, J.-H. ZHAO, C.-F. DUAN, L. HAO, and Y.-F. GUAN, "Thermal Desorption-Gas Chromatography or Gas Chromatography-Mass Spectrometry for Analysis of Semi-Volatile Compounds on Atmospheric Particulate Matters," *Chinese J. Anal. Chem.*, vol. 42, no. 7, pp. 931–936, 2014, doi: https://doi.org/10.1016/S1872-2040(14)60749-0.

[20] J. Pereira *et al.*, “Breath analysis as a potential and non-invasive frontier in disease diagnosis: an overview,” *Metabolites*, vol. 5, no. 1, pp. 3–55, Jan. 2015, doi: 10.3390/metabo5010003.

[21] A. M. Fosnight, B. L. Moran, and I. R. Medvedev, “Chemical analysis of exhaled human breath using a terahertz spectroscopic approach,” *Appl. Phys. Lett.*, vol. 103, no. 13, p. 133703, Sep. 2013, doi: 10.1063/1.4823544.

[22] C. F. Neese, I. R. Medvedev, G. M. Plummer, A. J. Frank, C. D. Ball, and F. C. De Lucia, “Compact Submillimeter/Terahertz Gas Sensor With Efficient Gas Collection, Preconcentration, and ppt Sensitivity,” *IEEE Sens. J.*, vol. 12, no. 8, pp. 2565–2574, 2012, doi: 10.1109/JSEN.2012.2195487.

[23] I. R. Medvedev, C. F. Neese, G. M. Plummer, and F. C. De Lucia, “Submillimeter spectroscopy for chemical analysis with absolute specificity,” *Opt. Lett.*, vol. 35, no. 10, pp. 1533–1535, 2010, doi: 10.1364/OL.35.001533.

[24] P. F. Bernath, *Spectra of Atoms and Molecules*. Oxford University Press, Inc, 1995.

[25] W. Gordy and R. L. Cook, *Microwave molecular spectra*, 3rd ed. New York: Wiley, 1984.

[26] C. N. Banwell and E. M. McCash, *Fundamentals of Molecular Spectroscopy*. McGraw-Hill, 1994.

[27] P. Kluczynski, J. Gustafsson, Å. M. Lindberg, and O. Axner, “Wavelength modulation absorption spectrometry — an extensive scrutiny of the generation of

signals," *Spectrochim. Acta Part B At. Spectrosc.*, vol. 56, no. 8, pp. 1277–1354, 2001, doi: https://doi.org/10.1016/S0584-8547(01)00248-8.

[28] P. Kluczynski and O. Axner, "Theoretical description based on Fourier analysis of wavelength-modulation spectrometry in terms of analytical and background signals," *Appl. Opt.*, vol. 38, no. 27, pp. 5803–5815, Sep. 1999, doi: 10.1364/AO.38.005803.

[29] S. Schilt, L. Thevenaz, and P. Robert, "Wavelength modulation spectroscopy: combined frequency and intensity laser modulation," *Appl. Opt.*, vol. 42, no. 33, pp. 6728–6738, Nov. 2003, doi: 10.1364/AO.42.006728.

[30] J. A. SILVER, "FREQUENCY-MODULATION SPECTROSCOPY FOR TRACE SPECIES DETECTION - THEORY AND COMPARISON AMONG EXPERIMENTAL METHODS," *Appl. Opt.*, vol. 31, no. 6, pp. 707–717, Feb. 1992, doi: 10.1364/AO.31.000707.

[31] J. M. SUPPLEE, E. A. WHITTAKER, and W. LENTH, "THEORETICAL DESCRIPTION OF FREQUENCY-MODULATION AND WAVELENGTH MODULATION SPECTROSCOPY," *Appl. Opt.*, vol. 33, no. 27, pp. 6294–6302, Sep. 1994, doi: 10.1364/AO.33.006294.

[32] R. ARNDT, "ANALYTICAL LINE SHAPES FOR LORENTZIAN SIGNALS BROADENED BY MODULATION," *J. Appl. Phys.*, vol. 36, no. 8, pp. 2522-, 1965, doi: 10.1063/1.1714523.

[33] M. L. Meade and I. of Electrical Engineers, *Lock-in Amplifiers: Principles and Applications*. P. Peregrinus, 1983.

[34] “Mass Flow Controller w/RS485 Standard and Alarm Functions.” [Online]. Available: https://www.omega.com/en-us/flow-instruments/flow-meters/mass-flow-meters/p/FMA6500-Series.

[35] “Pfeiffer MVP 006 diaphragm pump.” [Online]. Available: https://www.pfeiffer-vacuum.com/en/products/vacuum-generation/diaphragm-pumps/.

[36] CAMSCO, “CAMSCO Sorbent selection chart v 3.0,” 2009. [Online]. Available: https://camsco.com/pages/sorbent-selection-chart.

[37] “Pfeiffer HiPace 10.” [Online]. Available: https://www.pfeiffer-vacuum.com/en/products/vacuum-generation/turbopumps/hybrid-bearing/hipace-10/32021/hipace-10.

[38] “Virginia Diodes, Inc - Your Source for Terahertz and mm-Wave Products.” [Online]. Available: https://www.vadiodes.com/en/. [Accessed: 17-Dec-2019].

[39] “Mini Circuits ZX60-3011.” [Online]. Available: https://www.minicircuits.com/WebStore/dashboard.html?model=ZX60-3011%2B.

[40] “USB Lock-In Amplifier.” [Online]. Available: http://www.anfatec.com/Products/3_lockIn/USBLockIn/USB_Lock-In_Amplifier_250.html.

[41] “NI USB-6366 X Series.” [Online]. Available: https://www.ni.com/en-us/support/model.usb-6366.html.

[42] R. A. Serway and J. W. Jewett, *Physics for Scientists and Engineers, Chapters 1-39*. Cengage Learning, 2012.

[43] C. R. MacCluer, *A Survey of Industrial Mathematics*. Dover Publications, 2010.

[44] W. H. Press, B. P. Flannery, and S. A. Teukolsky, *Numerical recipes. The art of scientific computing*. 1986.

[45] "Formaldehyde Solution." [Online]. Available: https://www.sigmaaldrich.com/catalog/product/sial/252549?lang=en&region=US&cm_sp=Insite-_-caContent_prodMerch_gruCrossEntropy-_-prodMerch10-2.

[46] "Tedlar Gas Sampling Bag." [Online]. Available: http://www.celscientific.com/TedlarBag.html?gclid=Cj0KCQiA2af-BRDzARIsAIVQUOdpf7kBZ3epa8I_0TKrvKtGLzCgYNNkIxJ3mD7sb0vQ4mdMLmbeaUQaAtwwEALw_wcB.